


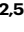


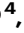






# Realization of Kagome Kondo lattice

Received: 27 November 2024

Accepted: 3 June 2025

Published online: 01 July 2025



Boqin Song <sup>1,5</sup>, Yuyang Xie<sup>1,2,5</sup>, Wei-Jian Li <sup>3,5</sup>, Hui Liu<sup>1</sup>, Jing Chen<sup>1</sup>, Shangjie Tian <sup>4</sup>, Xing Zhang<sup>1</sup>, Qinghong Wang<sup>1</sup>, Xintong Li <sup>1</sup>, Hechang Lei <sup>4</sup>, Qinghua Zhang <sup>1</sup>, Jian-gang Guo <sup>1</sup>, Lin Zhao <sup>1,2</sup>✉, Shun-Li Yu <sup>3</sup>✉, Xingjiang Zhou <sup>1,2</sup>, Xiaolong Chen<sup>1,2</sup>✉ & Tianping Ying <sup>1</sup>✉

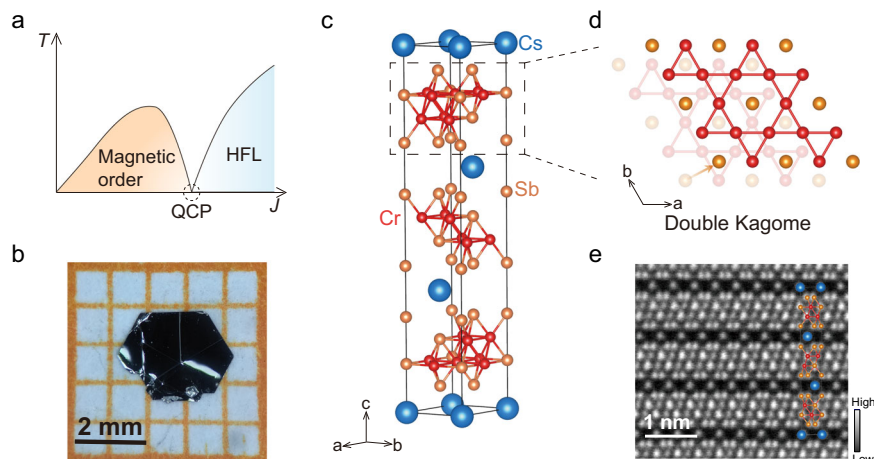
The Kondo lattice, describing a grid of the local magnetic moments coupling to itinerant electrons, is a fertile ground of strongly correlated states in condensed matter physics. While the Kagome lattice has long been predicted to host Kondo physics with exotic magnetism and nontrivial topology, no experimental realization has been achieved to the best of our knowledge. Here, we report the discovery of CsCr<sub>6</sub>Sb<sub>6</sub>, a van der Waals-like Kagome Kondo lattice featuring extremely flat, isolated bands at the Fermi level that composed entirely of Cr-3d electrons. We observe heavy fermions with the effective mass over 100 times greater than those of its vanadium counterpart. We also observe Kondo insulating behavior in an ultra-low carrier density of 10<sup>19</sup> cm<sup>-3</sup> and dimensionality-induced Kondo breakdown. Counterintuitively, mechanical exfoliation of the frustrated bulk reveals hidden A-type anti-ferromagnetism with even-odd layer-dependent anomalous Hall effect. The realization of Kondo physics in Kagome lattice opens avenues for exploring diverse quantum criticalities in a strongly-correlated frustrated system.

Kagome lattice, characterized by symmetry-protected Dirac points, van Hove singularities and flat bands, provides an exciting platform to intertwine nontrivial topology, frustrated magnetism and strongly correlated electrons<sup>1–16</sup>. However, accessing strong correlation effects in Kagome materials remains challenging, as their flat bands are often distant from  $E_F$  or disrupted by structural distortions that deviate from the ideal Kagome structure<sup>12–16</sup>. The canonical Kondo phase diagram (Fig. 1a) is typically realized in *f*-electron compounds, where strong correlations emerge from the interaction between two essential ingredients: itinerant electrons and local magnetic moments<sup>17–28</sup>. Recent observations of strange metallicity in Ni<sub>3</sub>In and pressurized CsCr<sub>3</sub>Sb<sub>5</sub> suggest that bringing portions of the Kagome flat bands closer to  $E_F$  could effectively enhance electronic correlations<sup>29–31</sup>, yet the absence of local moments in these systems precludes the development of Kondo physics. In contrast, Nb<sub>3</sub>Cl<sub>8</sub> exhibits local magnetic moments when its Kagome flat band approaches the Fermi level, but

the absence of itinerant electrons leads to a Mott insulating ground state<sup>32</sup>. Therefore, simultaneously bringing a dispersive band and a Kagome flat band to  $E_F$  is a promising route to realize a Kagome Kondo lattice.

In this article, we report the realization of a Kagome Kondo lattice in the van der Waals-like crystal CsCr<sub>6</sub>Sb<sub>6</sub>, which hosts extremely flat, isolated bands at the Fermi level, giving rise to heavy fermions with ultra-low carrier density and strong correlations in a non-*f*-electron system. Remarkably, as the material is thinned down to a few layers, its bulk magnetic frustration gives way to an emergent A-type anti-ferromagnetic order and layer-parity-dependent anomalous Hall response, a feature absent in conventional 2D magnets. These distinct phenomena arise from the delicate interplay between Kondo screening and RKKY interaction. Our findings establish CsCr<sub>6</sub>Sb<sub>6</sub> as a rare platform where frustration geometry, strong correlations, and tunable dimensionality converge to yield exotic quantum states.

<sup>1</sup>Beijing National Laboratory for Condensed Matter Physics, Institute of Physics, Chinese Academy of Sciences, Beijing, China. <sup>2</sup>School of Physical Sciences, University of Chinese Academy of Sciences, Beijing, China. <sup>3</sup>National Laboratory of Solid State Microstructures and Department of Physics, Nanjing University, Nanjing, China. <sup>4</sup>Department of Physics and Beijing Key Laboratory of Optoelectronic Functional Materials & MicroNano Devices, Renmin University of China, Beijing, China. <sup>5</sup>These authors contributed equally: Boqin Song, Yuyang Xie, Wei-Jian Li. ✉e-mail: [lzhao@iphy.ac.cn](mailto:lzhao@iphy.ac.cn); [slyu@nju.edu.cn](mailto:slyu@nju.edu.cn); [xlchen@iphy.ac.cn](mailto:xlchen@iphy.ac.cn); [ying@iphy.ac.cn](mailto:ying@iphy.ac.cn)



**Fig. 1 | Crystal and electronic structures of CsCrSb<sub>6</sub>.** **a** Illustration of the competing phases of heavy fermion liquid and magnetic ordered state. **b** Optical image of a CsCrSb<sub>6</sub> single crystal. **c** Crystal structure obtained from single crystal X-ray

diffraction. **d** Double Kagome structure viewed along the c-axis, with the bottom Kagome layer shown in varying transparency. **e** Atomic-resolution image of CsCrSb<sub>6</sub> viewed along the a-axis with the crystal structure superimposed.

## Results and discussion

### A Kagome Kondo lattice

Figure 1b shows the optical image of the Kagome material CsCrSb<sub>6</sub>, whose crystal structure is depicted in Fig. 1c (detailed single crystal characterization see Supplementary Fig. 1). Unlike other 166-Kagome materials such as RMn<sub>6</sub>Sn<sub>6</sub><sup>11</sup> and RV<sub>6</sub>Sn<sub>6</sub><sup>33</sup> (R = rare earth elements) that exhibit a three-dimensional (3D) nature, CsCrSb<sub>6</sub> is van der Waals like, featuring a space group of *R*-3m and lattice parameters *a* = 5.546(2) Å and *c* = 34.52(1) Å. Figure 1d illustrates the building blocks of the double Kagome (DK) layer. Successive three DK layers are shifted through [2/3, 1/3, 1/3] to form an ABC stacking lattice, each segregated by Cs atoms. Figure 1e presents an atomic-resolution scanning transmission electron microscopy (STEM) image with the superimposed crystal structure along the *a*-axis. CsCrSb<sub>6</sub> single crystals can be mechanically exfoliated into a single DK layer (~1.1 nm, namely 1/3 of the unit cell, see Supplementary Fig. 2). Additionally, we note that both single crystals and thin flakes of CsCrSb<sub>6</sub> are robust against moisture, greatly facilitating future characterization and manipulation.

Figure 2a presents the angle-resolved photoemission spectroscopy (ARPES) band structures along high-symmetry directions at 15 K. Notably, a dispersionless flat band is observed along the  $\Gamma$ -M and  $\Gamma$ -K high symmetry directions in momentum space, positioned right beneath  $E_F$ . Enlarged second derivative of band structures can be found in Supplementary Fig. 3. To further highlight the flat band feature, we plot the energy distribution curves (EDCs) within a narrower energy window in Fig. 2c. By tracing the EDCs peaks, as indicated by the red tips, the detailed band structure can be discerned. We find that the observed flat band feature is not a single band but consists of two bands around the  $\Gamma$  point. One band crosses the  $E_F$ , forming a small pocket around Brillouin zone center (as show in Fig. 2b), while the other is a dispersionless flat band situated around 40 meV below  $E_F$ , extending towards the K and M points. Around the K point, the flat band crosses  $E_F$ , forming a triangular pocket, while near the M point, the flat band just touches  $E_F$ , creating a prominent spot feature on the Fermi surface.

Another prominent observation is the presence of a band gap between the flat bands and valence bands, spanning from 50 meV to 0.5 eV. These findings make CsCrSb<sub>6</sub> stand out among other Kagome materials, where previously reported flat bands are either mixed with other bands, or positioned far from  $E_F$ .

Figure 2d presents a local-density-approximation (LDA) calculation of CsCrSb<sub>6</sub> without considering electron correlation, which

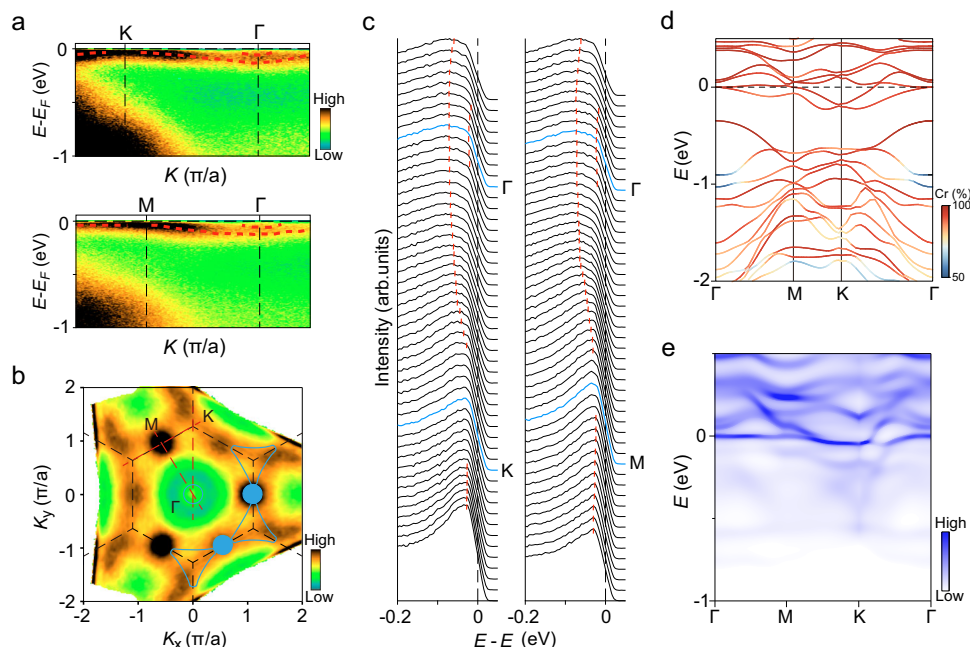
reveals a Kagome flat band located exactly at  $E_F$ . However, we notice that the calculated band dispersions do not align well with our ARPES measurements, particularly around the K point, indicating significant correlation within the system. We determined the renormalization factor by the ratio of experimental bandwidth (~40 meV) to that of calculated conduction band minimum relative to the  $E_F$ , which is significantly large, ~10, when comparing the ARPES experiments with theoretical calculations. To address this discrepancy, we employ dynamical mean field theory (DMFT) to renormalize the band structure, which successfully captures the features of the flat band at  $E_F$ , as shown in Fig. 2e. Notably, the orbital projection in Fig. 2d (detailed in Supplementary Fig. 4) shows that all bands near  $E_F$  are all primarily contributed by Cr's 3d electrons, confirming that the observed flat bands are pure Kagome bands. These flat bands suppress the kinetic energy of electrons, effectively localizing the magnetic moments of Cr, while residual pockets around the  $\Gamma$  point support mobile electrons.

We further carried out scanning tunneling microscopy (STM) and spectroscopy (STS) measurements to prove Kondo hybridization by decreasing the temperature. As shown in Supplementary Fig. 5, the STS spectra at 77 K show a metallic-like behavior with a finite density of states at the Fermi level. However, at 2 K, a clear gap opens around  $E_F$ , with the gap size estimated to be ~10–15 meV. This gap is consistent with the formation of a Kondo insulating state, where the hybridization between the localized Cr-3d electrons (flat band) and the itinerant electrons (dispersive band) leads to the opening of an energy gap. Therefore, CsCrSb<sub>6</sub> fulfill the requirements of a Kagome Kondo lattice.

### Heavy fermions with ultra-low charge carrier density

Figure 3a displays the temperature-dependent resistivity of a bulk sample. The large resistivity of CsCrSb<sub>6</sub> is intrinsic, as confirmed by measurements on three independent sample batches (Supplementary Fig. 6b). The high resistivity arises from the dominance of Kagome-derived flat bands near the Fermi level, which significantly suppress the kinetic energy of electrons. This contrasts with other Kagome metals, such as CsV<sub>3</sub>Sb<sub>5</sub>, where additional dispersive bands from non-Kagome lattices contribute to their metallicity. It exhibits metallic behavior at high temperatures and reaches a minimum. Upon further cooling, the resistance increases, showing a canonical  $-\log T$  divergence. This resistance minimum arises from enhanced scattering between local moments and itinerant electrons<sup>34</sup>, as described by

$$\rho = aT^5 + c\rho_0 - c\rho_1 \log T \quad (1)$$



**Fig. 2 | Extreme flat bands of CsCrSb<sub>6</sub>.** **a** Band structures measured along the  $\Gamma$ -K and  $\Gamma$ -M high symmetry directions in the momentum space at 15 K using He I lamp (21.2 eV). **b** Fermi surface mapping of CsCrSb<sub>6</sub> measured at 15 K. It is obtained by integrating the spectral intensity within 10 meV with respect to the  $E_F$ . The blue solid curves schematically depict the shape of Fermi surface. **c** Energy distribution curve (EDCs) of the photoemission spectra along the  $\Gamma$ -K and  $\Gamma$ -M high symmetry

directions. The EDCs at K and M points are highlighted. The red tips mark the EDC peaks to trace the band dispersions. **d** Density functional theory (DFT) calculation of CsCrSb<sub>6</sub> without considering electron correlation. Color variation represents the spectral weight percentage of Cr relative to the summation of Cr and Sb content. **e** Dynamical mean field theory (DMFT) result of a two-orbital model of CsCrSb<sub>6</sub> with  $U = 1.8$  eV.

Below  $T_K = 20$  K, the resistance deviates from the  $-\log T$  dependence and continue to increase with a mild slope, marking the formation of Kondo singlets and indicating the emergence of heavy fermions due to Kondo resonance.

To demonstrate this, we compare the heat capacity of CsCrSb<sub>6</sub> with its isostructural counterpart CsV<sub>6</sub>Sb<sub>6</sub> as shown in Fig. 3b, c. The extracted Sommerfeld coefficient  $\gamma_{\text{Cr-166}} = 75 \text{ mJ} \cdot \text{mol}^{-1} \cdot \text{K}^{-2}$  is three times larger than that of CsV<sub>6</sub>Sb<sub>6</sub>. Note that CsCrSb<sub>6</sub> exhibits insulating behavior at low temperatures with an ultra-low carrier density of  $10^{19} \text{ cm}^{-3}$  (as  $R_H$  shown in the inset of Fig. 3a, Hall measurements data and the carrier density extracted from Supplementary Figs. 6 and 7), in contrast to the metallic CsV<sub>6</sub>Sb<sub>6</sub> with a carrier density of  $10^{21} \text{ cm}^{-3}$ . This value is even lower than the rare low-carrier-density Kondo systems<sup>35–37</sup>, such as CeNi<sub>2</sub>As<sub>2</sub><sup>38</sup>. Calculation using the free electron gas model reveals a large effective mass for CsCrSb<sub>6</sub> of  $m^*/m_0 = 60$ , which is two orders of magnitude larger than that of CsV<sub>6</sub>Sb<sub>6</sub>. This value surpassing most *d*-electron systems on record and reaching the territory of *f*-electron heavy fermion materials<sup>39–45</sup> (Fig. 3d). Instead of a heavy fermion metal, the insufficient Kondo screening results in insulating-like behavior due to incoherent scattering, similar to observations in low-carrier-density *f*-electron systems CeNi<sub>2</sub>As<sub>2</sub> and NaYbSe<sub>2</sub><sup>46</sup>.

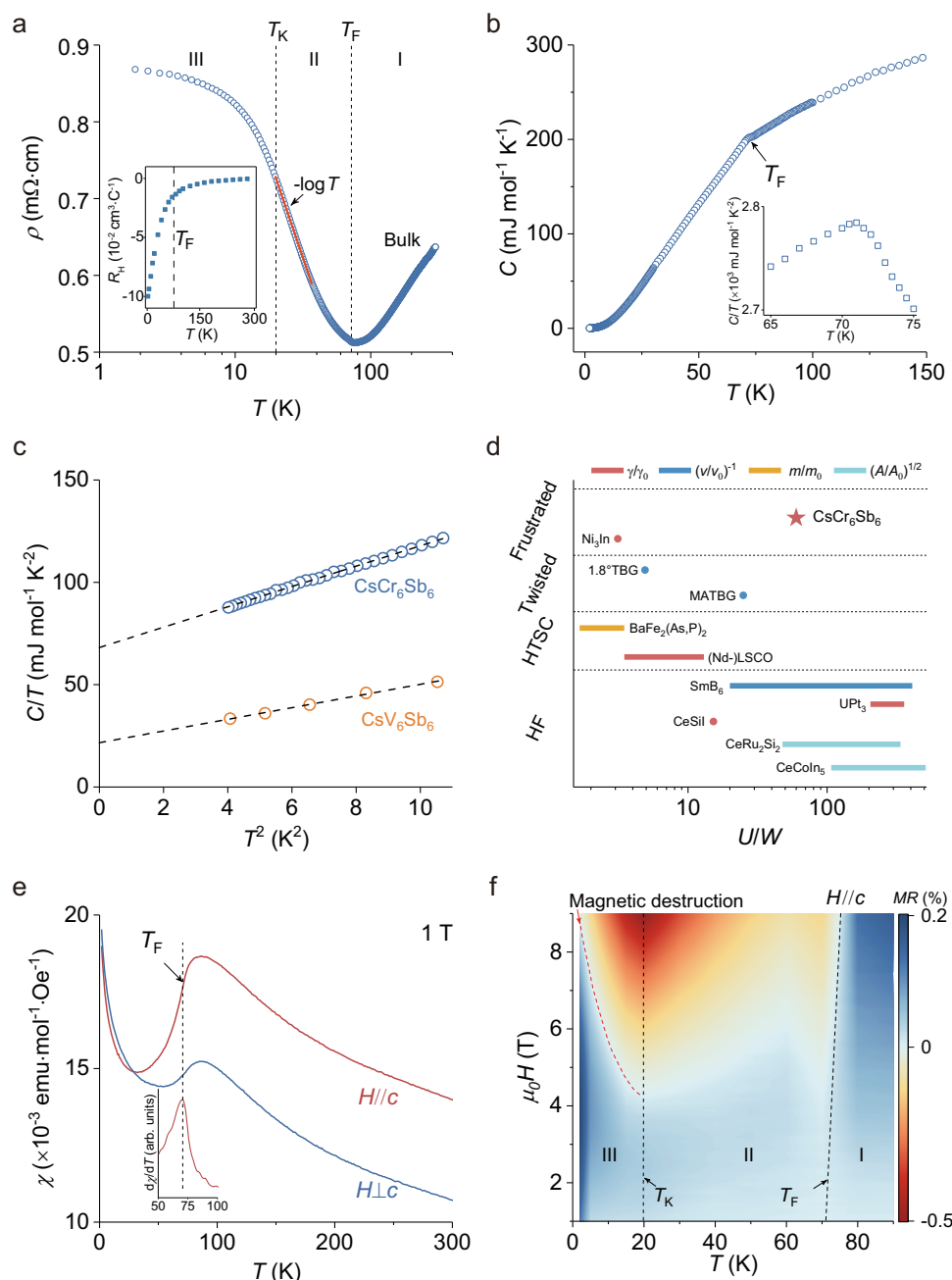
Notably, the resistivity exhibits an inconspicuous kink at  $T_F = 72$  K, which is more clearly visible in Supplementary Fig. 6a. This kink is related to a magnetic interaction, as indicated by the magnetization drop shown in Fig. 3e. Even though, no long-range magnetic order emerges due to the frustration inherent in the Kagome lattice, as evidenced by the broad hump in magnetization and the absence of the  $\lambda$ -type anomaly in heat capacity shown in Fig. 3b. Curie-Weiss fitting of the magnetic susceptibility reveal a magnetic moment of  $1.76 \mu_B$  per Cr (Supplementary Fig. 8). The fitted Neel temperature is much higher than  $T_F$ , suggesting the strong frustration. The origin of these short-range magnetic interactions remains unclear, potentially arising from the incomplete localization of wavefunction.

Next, we examine the impact of local moment screening on magnetotransport properties. Figure 3f shows the contour plot of magnetoresistance (MR) of the bulk sample at different temperatures. At  $T_F$ , a crossover from positive to negative MR is manifested, and its amplitude reaches a maximum at  $T_K$ . These two characteristic temperatures divide the behavior of MR into three regions. In region II, the negative MR can be attributed to the suppression of local moment scattering by external magnetic fields. In the III (below  $T_K$ ), the partial Kondo screening cancels out the negative MR caused by local moment scattering. The MR returns to negative at high magnetic fields, which can be attribute to the destruction of heavy fermions and the resurgence of the local moment scattering<sup>47</sup>. Magnetic destruction occurs when the Zeeman energy exceeds  $T_K$ , so the destruction field increases with cooling. The temperature-dependent MR behavior and magnetic destruction of heavy fermions observed in CsCrSb<sub>6</sub>, combined with the prominent enhancement of effective mass, verify the formation of Kondo resonance at  $T_K$ .

### Dimensionality induced Kondo breakdown

The van der Waals nature of CsCrSb<sub>6</sub> enables the exploration of dimensional reduction effects on the interplay of various emergent quantum phenomena, which is a long-standing aspiration in study of Kondo lattice physics but remains a significant challenge due to the 3D atomic and electronic structures of conventional heavy fermion compounds<sup>45,48,49</sup>. Recent results in exfoliated CeSiI suggest a small step towards this goal, despite the nearly unchanged Kondo temperature and coercive magnetic fields. Here, we demonstrate the successful tuning of  $T_K$  in CsCrSb<sub>6</sub> by exfoliating the bulk sample approaching its 2D limit.

Note that  $T_F$  is defined as the temperature at which the MR reverses sign (Supplementary Fig. 9), while  $T_K$  is at the maximum negative MR. Figure 4a, b shows MR at 9 T and  $dR/dT$  of CsCrSb<sub>6</sub> in bulk and 36 L sample, respectively. The high similarity of MR and  $dR/dT$  in both bulk and thin flakes indicates the two characteristic



**Fig. 3 | Frustrated magnetism and heavy fermion with ultra-low carrier density.**

**a** Resistance of bulk  $\text{CsCr}_6\text{Sb}_6$  single crystal. A kink at 72 K indicates the onset of frustrated magnetic state. The red line is a  $-\log T$  plot of resistivity, which gradually deviate from linear curve below  $T_K$ . Inset shows the temperature dependence of the Hall coefficient, which shows a drastic reduction at  $T_F$ . Three regions are divided by  $T_F$  and  $T_K$ . **b** Heat capacity ( $C_p$ ) of  $\text{CsCr}_6\text{Sb}_6$  shows a subtle kink at 72 K. Inset is the  $T$  dependent  $C_p/T$  curve around 72 K, revealing a broad hump at the same temperature. **c** Linear fitting of  $C_p/T$  versus  $T^2$ , the linear residual gives an electron contribution of  $75 \text{ mJ mol}^{-1} \text{ K}^{-2}$ . **d** Correlation strength of several correlated materials,

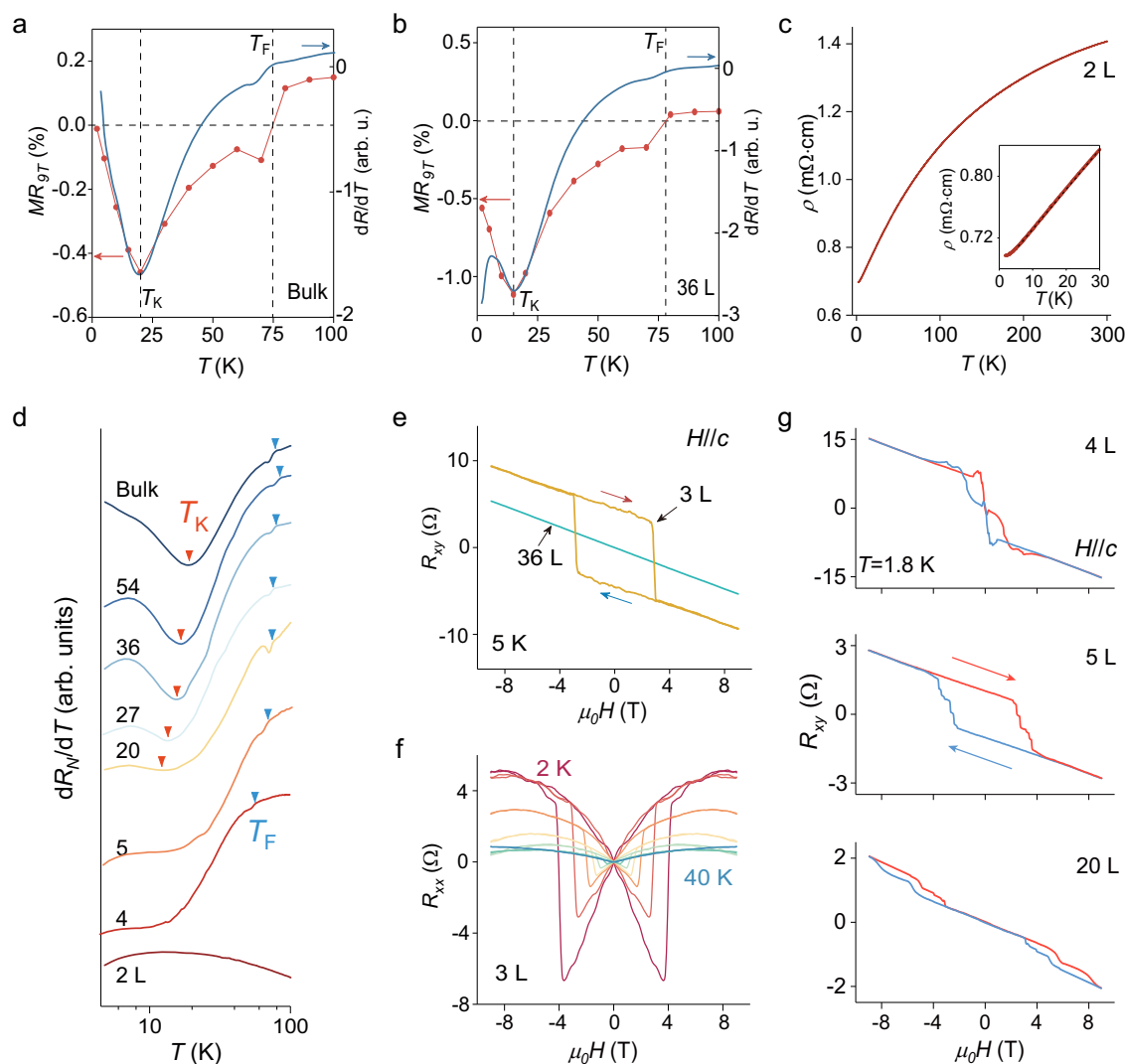
which places  $\text{CsCr}_6\text{Sb}_6$  within the realm of  $f$ -electron heavy fermions<sup>17,39–45</sup>. HTSC and HF are short for high temperature superconductors and heavy fermion materials, respectively. **e** Magnetic susceptibility  $\chi$  of  $\text{CsCr}_6\text{Sb}_6$  measured along and perpendicular to the  $c$ -axis. The  $d\chi/dT$  curve shown in the inset peaks at 72 K, consistent with the observed  $T_F$  shown in (a). **f** Contour plot of MR, divided into three regions same to (a). Region II and III are dominated by moments and singlets scattering, respectively. Dashed line in region III marks the boundary of magnetic destruction. Magnetic field is along  $c$ -axis.

temperatures are both reflected in the resistance behavior. Based on this, we depict the dimensionality effect on the Kondo exchange ( $J_K$ ) in  $\text{CsCr}_6\text{Sb}_6$  by fabricating devices with thickness varies from bulk to 2 L (Fig. 4d). The  $dR/dT$  data are renormalized and shifted for clarity. We observe that  $T_K$  can be feasibly tuned as the sample thickness is reduced to tens of nanometers, exhibiting a monotonic decrease. These results suggest that dimensional reduction diminishes the  $J_K$ , which is consistent with the general recognition of weakened Coulomb

screening approaching the 2D limit. The hopping of conduction electrons is thus suppressed, exacerbating the insufficient Kondo screening. Meanwhile the quantum fluctuations raised by dimensional reduction may also destabilize the singlets.

In the 36 L sample, MR measurement indicates that the magnetic destruction field is 2.8 T at 1.8 K (Supplementary Fig. 10d), significantly lower than the 8.7 T observed in the bulk (Fig. 3f), verifying the reduced energy scale of  $J_K$ . By further reducing the thickness to 5 L, the





**Fig. 4 | Highly tunable  $T_K$  and a hidden AFM state.** **a, b** MR at 9 T and  $dR/dT$  of the bulk and the 36 L sample, respectively. Both bulk and thin flakes exhibit a kink and a minimum in  $dR/dT$  coinciding with  $T_F$  and  $T_K$ . **c** Temperature dependent resistivity of 2 L sample, with residual resistivity of 700  $\mu\Omega$ ·cm. Inset show the linear dependence of the resistivity at low temperature. **d**  $dR/dT$  of samples with varying thickness from bulk to 2 DK layers (2 L, hereafter). The curves are normalized and vertically offset for clarity.  $T_K$  and  $T_F$  are indicated by blue and red triangles, respectively.

respectively. **e** Hall resistance  $R_{xy}$  of 3 and 36 L samples. A hysteresis and anomalous Hall resistance appear in the 3 L sample with a coercive field of 3.8 T. **f** temperature dependent MR of the 3 L sample, where the critical temperature is defined as the temperature at which the hysteresis vanishes. **g**  $R_{xy}$  of samples with thickness of 4, 5 and 20 L. red and blue lines represent up and down sweep of the magnetic field. Even-layer samples exhibit AFM states, while odd-layer ones are in a ferromagnetic (FM) state. Magnetic fields are all along  $c$ -axis.

minimum of  $dR/dT$  vanishes, indicating a complete suppression of  $J_K$  and the realization of a dimensionality-induced Kondo breakdown. Meanwhile,  $T_F$  persists and continues to shift toward lower temperatures. Interestingly, in the region of complete Kondo breakdown, the 2 L sample exhibits strange metal behavior with a residual resistivity exceeding 700  $\mu\Omega$ ·cm (Fig. 4c), highlighting a unique dimensional effect as the system approaches the atomic limit.

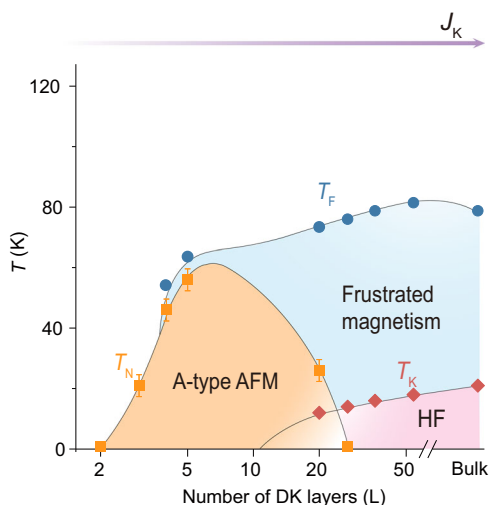
### Hidden magnetic ordered states

In a Kondo lattice, the Ruderman–Kittel–Kasuya–Yosida (RKKY) interaction is generally suppressed by Kondo screening. A key distinction between Kondo lattices and impurity Kondo effect is the realization of long-range magnetic ordered states by tuning various parameters. As we have established the dimensionality tuned  $J_K$ , we further investigate the magnetic response of this Kagome Kondo lattice, particularly near the Kondo breakdown, through magneto-transport measurements.

As expected, we observe the emergence of a long-range antiferromagnetic ordered state below ~20 L, which is absent in the bulk.

For comparison, we plot the transverse resistance  $R_{xy}$  of 3 L and 36 L thin flakes at 5 K in Fig. 4e. Distinct from the 36 L and bulk samples,  $R_{xy}$  of 3 L sample shows prominent jumps at 2.5 T and display hysteresis upon sweeping the magnetic fields. Notably, the anomalous Hall resistance observed at zero field indicates the formation of a ferromagnetic ground state with the easy axis oriented out-of-plane (Supplementary Fig. 11). The temperature dependent MR of the 3 L sample shows the characteristic butterfly hysteresis of ferromagnetism (Fig. 4f).

The odd and even DK layers provide further insights into the magnetic structure. As shown in Fig. 4g, the even-layer samples exhibit antiferromagnetic hysteresis, while the odd-layer samples display ferromagnetic loops. This even-odd-layer-dependent behavior is a hallmark of A-type antiferromagnetism. Consequently, the magnetic unit cell of CsCrSb<sub>6</sub> should contain at least six DK layers. Meanwhile, the magnetic ordering within each DK and its thickness evolution remains unclear thus far. Moreover, the  $R_{xy}$  of few-layers CsCrSb<sub>6</sub> flakes show a lot of steps at lower temperatures (additional temperature-dependent



**Fig. 5 | Magnetic phase diagram.** Blue circle and pink diamonds are  $T_F$  and  $T_K$ , respectively. Squares represent the AFM magnetic transition  $T_N$ , which is determined as the temperature at which the magnetization-induced jumps in MR or  $R_{xy}$  vanish. Error bars are defined by the temperature steps in MR measurements. The thickness of the samples tunes  $J_K$  driving the system from a frustrated state in the bulk into a long-range AFM ordered state with dimension reduction down to few layers.

$R_{xy}$  data are presented in Supplementary Figs. 12 and 13), suggesting more complex magnetic states or domain structures compared to those observed in  $\text{MnBi}_2\text{Te}_4$ <sup>50</sup> and  $\text{MnBi}_4\text{Te}_7$ <sup>51</sup>, warranting further investigation.

This finding is unique from the perspective of 2D magnetism. Recently search for 2D magnetic materials have focused on van der Waals compounds with high Curie or Néel temperatures and strong magnetocrystalline anisotropy to maintain magnetic order approaching their monolayer limit<sup>52–54</sup>.  $\text{CsCr}_6\text{Sb}_6$  is the only known example of emergent magnetism upon thinning, to the best of our knowledge. This peculiar thickness-dependent magnetism can now be fully understood within a unified framework of Kondo phase diagram.

As shown in Fig. 5, the blue circles and pink diamonds are  $T_F$  and  $T_K$ , and the orange squares represent the onset of magnetic ordering at  $T_N$ , determined as the temperature at which the magnetization-induced jumps in MR or  $R_{xy}$  vanish. In the bulk, the strong geometric frustration of the Kagome lattice prevents the formation of long-range antiferromagnetic order, which may promote the emergence of the heavy fermions; otherwise, the ground states of the bulk would enter the AFM phase. In the 20 L sample, the emergence of ordered states cannot totally suppress  $T_K$ . The Kondo screening occurring in an AFM state extends beyond the Doniach phase diagram, where typically only one phase dominates. The moisture stability of few-layer  $\text{CsCr}_6\text{Sb}_6$  further underscores its potential as a leading candidate for next-generation spintronic devices.

In conclusion, Kagome Kondo lattice has been experimentally realized in  $\text{CsCr}_6\text{Sb}_6$ . The discovery of heavy fermion behavior, Kondo singlets, Kondo breakdown, frustrated magnetic states, and a hidden AFM ordering establishes  $\text{CsCr}_6\text{Sb}_6$  as an ideal archetype for investigating various strongly-correlated phenomena. Emergent phenomena including quantum critical point, non-Fermi liquid behavior, heavy fermion superconductivity and high-temperature fractional quantum Hall states are waiting to be explored.

## Methods

### Crystal synthesis and characterization

Single crystalline  $\text{CsCr}_6\text{Sb}_6$  was synthesized using self-flux method. The mixture of Cs ingot (99.9%, Alfa), Cr grains (99.9%, Alfa) and Sb

powder (99.999%, Alfa) were weighted with the mole ratio of 10:3:30, loaded into an alumina crucible and sealed in a quartz ampoule. The ampoule was heated to 1223 K and soaked there for 24 h. Then it was cooled down to 923 K at a rate of 2 K/h followed by furnace cooling. Finally, the collected melt was immersed in water and the van-der-Waals-like hexagonal crystals were harvested with typical size of  $3\text{ mm} \times 3\text{ mm} \times 50\text{ }\mu\text{m}$ . Single crystal diffraction data was collected using a Rigaku XtaLAB Synergy R diffractometer (Supplementary Fig. 1a, resolved structure in Supplementary Table 1). X-ray diffraction (XRD) was performed on a Rigaku Smart Lab diffractometer with  $\text{Cu K}\alpha$  radiation ( $\lambda = 1.5418\text{ }\text{\AA}$ ) (Supplementary Fig. 1b). The magnetic properties were measured by a magnetism property measurement system (MPMS, Quantum Design). The high-angle annular dark-field (HAADF) images were captured using a JEOL ARM-200F scanning transmission electron microscope (STEM) operating at 200 Kv (Supplementary Fig. 1d). For structural analysis, the sample was prepared using the focused ion beam (FIB) method.

### High resolution ARPES measurements

High resolution angle-resolved photoemission measurements were performed using a lab-based ARPES system equipped with the 21.2 eV He I lamp and a hemispherical electron energy analyzer DA30L (Scienta-Omicron). The energy resolution was set at 20 meV. All the samples were cleaved in situ at 15 K and measured in ultrahigh vacuum with a base pressure better than  $5 \times 10^{-11}$  mbar. The Fermi level is referenced by measuring clean polycrystalline gold that is electrically connected to the sample.

### Fabrication and characterization of few-layer $\text{CsCr}_6\text{Sb}_6$ devices

We obtain few-layer  $\text{CsCr}_6\text{Sb}_6$  samples using an  $\text{Al}_2\text{O}_3$ -assisted exfoliation technique as described in ref. 53. Firstly, the bulk samples are exfoliated to expose a fresh surface using scotch tapes. Then, 60–90 nm  $\text{Al}_2\text{O}_3$  is deposited on the surface. Next, the stack was picked up by a thermal-released tape. Through this process, few layer samples are exfoliated benefit from the tight adhesion between sample surface and  $\text{Al}_2\text{O}_3$ . Subsequently, the stamp of  $\text{Al}_2\text{O}_3/\text{CsCr}_6\text{Sb}_6$  is released onto a piece of PDMS (polydimethylsiloxane) with the  $\text{CsCr}_6\text{Sb}_6$  side in contact with the PDMS surface. Supplementary Fig. 2a shows a typical optical image of few-layer  $\text{CsCr}_6\text{Sb}_6$  samples on PDMS. Sample thickness is determined using the atomic force microscope and the optical contrast. Here, the optical contrast is transmittance defined as  $G_{\text{sample}}^T / G_{\text{substrate}}^T$ , where  $G_{\text{sample}}^T$  and  $G_{\text{substrate}}^T$  are the intensity of the transmission through the sample and substrate, respectively, in blue channel of the image captured with a charge-coupled device (CCD) camera. The transmittance of various numbers of layers follows the Beer-Lambert Law (Supplementary Fig. 2b) which enables us to determine the layer number quickly and precisely. After that, selected samples are finally stamped assembly onto a silicon substrate coated with 300 nm  $\text{SiO}_2$ . The electrical transport devices are fabricated through a standard electron beam lithography (EBL) process and a metal deposition with 5/60 nm Cr/Au as the electrodes.

### Data availability

Most relevant data generated in this study (Figs. 2–4) are provided in the Source Data file. All other data that support the findings of this study are available from the corresponding authors upon request. Source data are provided with this paper.

## References

1. Norman, M. R. Colloquium: Herbertsmithite and the search for the quantum spin liquid. *Rev. Mod. Phys.* **88**, 041002 (2016).
2. Sachdev, S. Kagome- and triangular-lattice Heisenberg antiferromagnets: ordering from quantum fluctuations and quantum-disordered ground states with unconfined bosonic spinons. *Phys. Rev. B* **45**, 12377–12396 (1992).

3. Tang, E., Mei, J.-W. & Wen, X.-G. High-temperature fractional quantum Hall states. *Phys. Rev. Lett.* **106**, 236802 (2011).
4. Yan, S., Huse, D. A. & White, S. R. Spin-liquid ground state of the  $S=1/2$  kagome Heisenberg antiferromagnet. *Science* **332**, 1173–1176 (2011).
5. Han, T.-H. et al. Fractionalized excitations in the spin-liquid state of a kagome-lattice antiferromagnet. *Nature* **492**, 406–410 (2012).
6. Ye, L. D. et al. Massive Dirac fermions in a ferromagnetic kagome metal. *Nature* **555**, 638–642 (2018).
7. Yin, J. X. et al. Giant and anisotropic many-body spin–orbit tunability in a strongly correlated kagome magnet. *Nature* **562**, 91–95 (2018).
8. Morali, N. et al. Fermi-arc diversity on surface terminations of the magnetic Weyl semimetal  $\text{Co}_3\text{Sn}_2\text{S}_2$ . *Science* **365**, 1286–1291 (2019).
9. Liu, D. F. et al. Magnetic Weyl semimetal phase in a Kagomé crystal. *Science* **365**, 1282–1285 (2019).
10. Kuroda, K. et al. Evidence for magnetic Weyl fermions in a correlated metal. *Nat. Mater.* **16**, 1090 (2017).
11. Yin, J. X. et al. Quantum-limit Chern topological magnetism in  $\text{TbMn}_6\text{Sn}_6$ . *Nature* **583**, 533–536 (2020).
12. Yin, J.-X. et al. Negative flat band magnetism in a spin–orbit-coupled correlated kagome magnet. *Nat. Phys.* **15**, 443–448 (2019).
13. Kang, M. et al. Dirac fermions and flat bands in the ideal kagome metal  $\text{FeSn}$ . *Nat. Mater.* **19**, 163–169 (2020).
14. Ortiz, B. R. et al.  $\text{CsV}_3\text{Sb}_5$ : a  $z_2$  topological kagome metal with a superconducting ground state. *Phys. Rev. Lett.* **125**, 247002 (2020).
15. Chen, H. et al. Roton pair density wave in a strong-coupling kagome superconductor. *Nature* **599**, 222–228 (2021).
16. Zhao, H. et al. Cascade of correlated electron states in the kagome superconductor  $\text{CsV}_3\text{Sb}_5$ . *Nature* **599**, 216–221 (2021).
17. Gegenwart, P., Si, Q. & Steglich, F. Quantum criticality in heavy-fermion metals. *Nat. Phys.* **4**, 186–197 (2008).
18. Jiao, L. et al. Chiral superconductivity in heavy-fermion metal  $\text{UTe}_2$ . *Nature* **579**, 523–527 (2020).
19. Ernst, S. et al. Emerging local Kondo screening and spatial coherence in the heavy-fermion metal  $\text{YbRh}_2\text{Si}_2$ . *Nature* **474**, 362–366 (2011).
20. Aynajian, P. et al. Visualizing heavy fermions emerging in a quantum critical Kondo lattice. *Nature* **486**, 201–206 (2012).
21. Allan, M. P. et al. Imaging Cooper pairing of heavy fermions in  $\text{CeCoIn}_5$ . *Nat. Phys.* **9**, 468–473 (2013).
22. Park, T. et al. Hidden magnetism and quantum criticality in the heavy fermion superconductor  $\text{CeRhIn}_5$ . *Nature* **440**, 65–68 (2006).
23. Zhou, B. B. et al. Visualizing nodal heavy fermion superconductivity in  $\text{CeCoIn}_5$ . *Nat. Phys.* **9**, 474–479 (2013).
24. Doniach, S. The Kondo lattice and weak antiferromagnetism. *Phys. B + C* **91**, 231 (1977).
25. Kirchner, S. et al. Colloquium: heavy-electron quantum criticality and single-particle spectroscopy. *Rev. Mod. Phys.* **92**, 011002 (2020).
26. Checkelsky, J. G. et al. Flat bands, strange metals and the Kondo effect. *Nat. Rev. Mater.* **9**, 509–526 (2024).
27. Stewart, G. R. Non-Fermi-liquid behavior in  $d$ - and  $f$ -electron metals. *Rev. Mod. Phys.* **73**, 797–855 (2001).
28. Paschen, S. & Si, Q. Quantum phases driven by strong correlations. *Nat. Rev. Phys.* **3**, 9–26 (2021).
29. Ye, L. et al. Hopping frustration-induced flat band and strange metallicity in a kagome metal. *Nat. Phys.* **20**, 610–614 (2024).
30. Liu, Y. et al. Superconductivity under pressure in a chromium-based kagome metal. *Nature* **632**, 1032–1037 (2024).
31. Wang, Y. Heavy-fermions in frustrated Hund’s metal with portions of incipient flat-bands. *Phys. Rev. B* **111**, 035127 (2025).
32. Gao, S. et al. Discovery of a single-band Mott insulator in a van der Waals flat-band compound. *Phys. Rev. X* **13**, 041049 (2023).
33. Hu, Y. et al. Phonon promoted charge density wave in topological kagome metal  $\text{ScV}_6\text{Sn}_6$ . *Nat. Commun.* **15**, 1658 (2024).
34. Kondo, J. Resistance minimum in dilute magnetic alloys. *Prog. Theor. Phys.* **32**, 37 (1964).
35. Feng X.-Y. et al. Dirac-Kondo semimetals and topological Kondo insulators in the dilute carrier limit. Preprint at <https://arxiv.org/abs/1605.02380> (2016).
36. Zhang, G.-M., Yang, Y.-F. & Zhang, F.-C. Self-doped Mott insulator for parent compounds of nickelate superconductors. *Phys. Rev. B* **101**, 020501 (2020).
37. Yang, Y. F. & Zhang, G. M. Self-doping and the Mott-Kondo scenario for infinite-layer nickelate superconductors. *Front. Phys.* **9**, 801236 (2022).
38. Chen, J. et al. Heavy fermion quantum criticality at dilute carrier limit in  $\text{CeNi}_{2-x}(\text{As}_{1-x}\text{P}_x)_2$ . *Sci. Rep.* **9**, 12307 (2019).
39. Cao, Y. et al. Correlated insulator behaviour at half-filling in magic-angle graphene superlattices. *Nature* **556**, 80–84 (2018).
40. Pirie, H. et al. Imaging emergent heavy Dirac fermions of a topological Kondo insulator. *Nat. Phys.* **16**, 52 (2020).
41. Cao, Y. et al. Superlattice-induced insulating states and valley-protected orbits in twisted bilayer graphene. *Phys. Rev. Lett.* **117**, 116804 (2016).
42. Shishido, H. et al. Evolution of the Fermi surface of  $\text{BaFe}_2(\text{As}_{1-x}\text{P}_x)_2$  on entering the superconducting dome. *Phys. Rev. Lett.* **104**, 057008 (2010).
43. Legros, A. et al. Universal T-linear resistivity and Planckian dissipation in overdoped cuprates. *Nat. Phys.* **15**, 142 (2019).
44. Taupin, M. & Paschen, S. Are heavy fermion strange metals Planckian?. *Crystals* **12**, 251 (2022).
45. Posey, V. A. et al. Two-dimensional heavy fermions in the van der Waals metal  $\text{CeSi}$ . *Nature* **625**, 483–488 (2024).
46. Xu, Y., Sheng, Y. & Yang, Y. F. Mechanism of the insulator-to-metal transition and superconductivity in the spin liquid candidate  $\text{NaYbSe}_2$  under pressure. *npj Quantum Mater.* **7**, 21 (2022).
47. Kitagawa, S. et al. Metamagnetic behavior and Kondo breakdown in heavy-fermion  $\text{CeFePO}$ . *Phys. Rev. Lett.* **107**, 277002 (2011).
48. Shishido, H. et al. Tuning the dimensionality of the heavy fermion compound  $\text{CeIn}_3$ . *Science* **327**, 980–983 (2010).
49. Mizukami, Y. et al. Extremely strong-coupling superconductivity in artificial two-dimensional Kondo lattices. *Nat. Phys.* **7**, 849–853 (2011).
50. Deng, Y. et al. Quantum anomalous Hall effect in intrinsic magnetic topological insulator  $\text{MnBi}_2\text{Te}_4$ . *Science* **367**, 895–900 (2020).
51. Xu, X. et al. Ferromagnetic-antiferromagnetic coexisting ground state and exchange bias effects in  $\text{MnBi}_4\text{Te}_7$  and  $\text{MnBi}_6\text{Te}_{10}$ . *Nat. Commun.* **13**, 7646 (2022).
52. Huang, B. et al. Layer-dependent ferromagnetism in a van der Waals crystal down to the monolayer limit. *Nature* **546**, 270–273 (2017).
53. Deng, Y. et al. Gate-tunable room-temperature ferromagnetism in two-dimensional  $\text{Fe}_3\text{GeTe}_2$ . *Nature* **563**, 94–99 (2018).
54. Liu, F. et al. Disassembling 2D van der Waals crystals into macroscopic monolayers and reassembling into artificial lattices. *Science* **367**, 903–906 (2020).

## Acknowledgements

This work is financially supported by the National Key Research and Development Program of China (No. 2021YFA1401800, 2022YFA1403900), National Natural Science Foundation of China (No. 52272267, 52202342, 52250308). This work was supported by the Synergetic Extreme Condition User Facility (SECUF). Chinese Academy of Sciences President’s International Fellowship Initiative. Grant No. 2025PD0005. A portion of numerical computations were carried out at the Hefei Advanced Computing Center.

## Author contributions

T.P.Y. and X.L.C. conceptualized the idea. B.Q.S. carried out the majority of sample synthesis, device fabrication, measurements, and data

processing, with assistance from H.L., S.J.T., H.C.L. and J.-G.G. J.C. and Q.H.Z. performed the electron diffraction. Y.Y.X., L.Z. and X.J.Z. carried out the ARPES measurements. X.Z., Q.H.Z. and X.T.L. performed STM measurements. W.-J.L. and S.-L.Y. performed the theoretical calculations. B.Q.S. and T.P.Y. analyzed the data and wrote the paper with inputs from all authors.

### Competing interests

The authors declare no competing interests.

### Additional information

**Supplementary information** The online version contains supplementary material available at <https://doi.org/10.1038/s41467-025-60785-3>.

**Correspondence** and requests for materials should be addressed to Lin Zhao, Shun-Li Yu, Xiaolong Chen or Tianping Ying.

**Peer review information** *Nature Communications* thanks Jungseek Hwang, Dalmau Reig-i-Plessis and the other, anonymous, reviewer(s) for their contribution to the peer review of this work. A peer review file is available.

**Reprints and permissions information** is available at <http://www.nature.com/reprints>

**Publisher's note** Springer Nature remains neutral with regard to jurisdictional claims in published maps and institutional affiliations.

**Open Access** This article is licensed under a Creative Commons Attribution-NonCommercial-NoDerivatives 4.0 International License, which permits any non-commercial use, sharing, distribution and reproduction in any medium or format, as long as you give appropriate credit to the original author(s) and the source, provide a link to the Creative Commons licence, and indicate if you modified the licensed material. You do not have permission under this licence to share adapted material derived from this article or parts of it. The images or other third party material in this article are included in the article's Creative Commons licence, unless indicated otherwise in a credit line to the material. If material is not included in the article's Creative Commons licence and your intended use is not permitted by statutory regulation or exceeds the permitted use, you will need to obtain permission directly from the copyright holder. To view a copy of this licence, visit <http://creativecommons.org/licenses/by-nc-nd/4.0/>.

© The Author(s) 2025